US-Taiwan Workshop on Smart Structural Technology for Seismic Hazard Mitigation

Taipei, Taiwan
October 12-14, 2006

Paper NO: 007

Debonding Monitoring of CFRP Strengthened RC Beams based on a Time Reversal Process of Guided Waves

Hoon Sohn[1], Seung Dae Kim[2], Chi Won In[3], Kelly E. Cronin[4] and Kent Harries[5]

ABSTRACT

Abstract: This study attempts to develop a real-time debonding monitoring system for carbon fiber-reinforced polymer (CFRP) strengthened structures by continuously inspecting the bonding condition between the CFRP layer and the host structure. The uniqueness of this study is in developing a new concept and theoretical framework of nondestructive testing (NDT), in which debonding is detected *without relying on previously-obtained baseline data*. The proposed reference-free damage diagnosis is achieved based on the concept of time reversal acoustics (TRA). In TRA, an input signal at an excitation point can be reconstructed if the response signal measured at another point is reemitted to the original excitation point after being reversed in the time domain. Examining the deviation of the reconstructed signal from the known initial input signal allows instantaneous identification of damage without requiring a baseline signal representing the undamaged state for comparison. The concept of TRA has been extended to guided wave propagations within the CFRP-strengthened reinforced concrete (RC) beams to improve the detectability of local debonding. Monotonic and fatigue load tests of large-scale CFRP-strengthened RC beams are conducted to demonstrate the potential of the proposed reference-free debonding monitoring system. Comparisons with an electro-mechanical impedance method and an inferred imaging technique are provided as well.

Keywords: active sensing, baseline-free nondestructive testing, carbon fiber reinforced polymer, debonding, structural health monitoring, time-reversal acoustics.

INTRODUCTION

Carbon fiber reinforced polymer (CFRP) composite materials have become an attractive alternate material for retrofit and rehabilitation of civil infrastructure systems due to their outstanding strength, light weight and versatility (Karbhari et al. 2000). However, the improvement of strength and stiffness in a host structure can only be guaranteed when a reliable bonding condition between the host structure and the added CFRP materials is maintained. Therefore, a reliable nondestructive testing (NDT) system is required to monitor the initial installation quality and the long-term efficiency of bonding.

There is a large volume of research on damage detection techniques for FRP strengthened concrete structures. To name a few, acoustic emission (Mirmiran et al. 1999), ultrasonic pulse velocities

[1] Assistant Professor, Carnegie Mellon Univ., Pittsburgh, PA 15213, Email: hsohn@cmu.edu
[2] Ph.D. Candidate, Carnegie Mellon Univ., Pittsburgh, PA 15213, Email: seungdak@andrew.cmu.edu
[3] Master Student, Carnegie Mellon Univ., Pittsburgh, PA 15213, Email: cin@andrew.cmu.edu
[4] Undergraduate Student, Carnegie Mellon Univ., Pittsburgh, PA 15213, Email: kcronin@andrew.cmu.edu
[5] Assistant Professor, Univ. of Pittsburgh, Pittsburgh, PA 15261, Email: kharries@engr.pitt.edu

(Mirmiran and Wei 2001), infrared thermography (Levar and Hamilton 2003), fiber optic sensing (Ansari 2005), electromechanical impedance spectrum (Giurgiutiu et al. 2003), electrochemical impedance spectroscopy methods (Hong and Harichandran 2005), and microwave sensing (Akuthota et al. 2004, Ekenel et al. 2004, Feng et al. 2000a) have been applied. These techniques are shown to successfully identify FRP debonding. However, data interpretation often needs to be manually performed by experienced engineers, and automation of data analysis remains largely unsolved. For continuous monitoring, it will be critical to reduce unnecessary interference by users and to automate the data analysis process as much as possible. In addition, although many damage detection techniques are successfully applied to scaled models or specimens tested in controlled laboratory environments, the performance of these techniques in real operational environments is still questionable and needs to be validated. Varying environmental and operational conditions produce changes in the system's dynamic response that can be easily mistaken for damage (Sohn 2006). It is challenging to develop a NDT technique with minimal false positive and negative indications of damage when the system is exposed to varying environmental and operational conditions. Few NDT systems have been developed with the intent of deploying it for continuous monitoring for in-service structures.

The ultimate goal of this study is to develop an NDT technique that goes beyond the laboratory demonstration and can be deployed in the field on real-world structures. To achieve this goal, a new NDT technique is developed by applying the concept of time reversal acoustics (TRA) (Fink and Prada 2001) to guided wave propagations (Rose 1999 and Viktorov 1967) within CFRP-strengthened RC beams. Based on TRA, an input signal at an excitation point can be reconstructed if the response signal measured at another point is reemitted to the original excitation point after being reversed in the time domain. This time reversibility is based on linear reciprocity of elastic waves, and breaks down when there is a source of nonlinearity along the wave propagation path. Because certain types of defects introduce nonlinear responses, examining the deviation of the reconstructed signal from the known initial input signal allows instantaneous identification of damage without requiring a direct comparison with previously-obtained baseline signal data. This novel concept is extended to develop a NDT system that can be rapidly deployed on laboratory specimens or in-field structures and autonomously perform local damage diagnoses at the presence of operational and environmental variation that in-service structures encounter. Smart materials such as lead zirconate titanate (PZT) are used for both generating and measuring guided waves (Giurgiutiu and Lyshevski 2004).

WAVE PROPAGATION IN TARGET STRUCTURES AND TIME REVERSAL ACOUSTICS

Elastic waves propagating in solid media can be classified into body and guided waves. All elastic waves including body and guided waves are governed by the same sets of Navier's partial differential equations (Rose 1999). The primary difference is that, while body waves are not constrained by any boundaries, guided waves need to satisfy the boundary conditions imposed by the physical systems as well as the governing equations. Guided waves can be further divided into Lamb, Stoneley and Rayleigh surface waves depending on specifics of the imposed boundary conditions.

Lamb waves are one type of guided waves that are constrained by two closely-spaced free surfaces (Viktorov 1967). In spite of its unique dispersion and multimode characteristics shown in Figure 1, Lamb waves are widely used for defect detection in NDT applications due to their relatively long sensing range (Ing and Fink 1996, Kessler et al. 2003, Kim et al. 2005, Mal et al. 2005 and Sohn et al. 2005). However, as the thickness of the plate (or the product of the exciting frequency (*f*) and the thickness of the plate (*d*) in Figure 1) increases, it becomes very hard to distinguish wave components because the fundamental symmetric (S_0) and anti-symmetric (A_0) Lamb modes converge to a Rayleigh surface wave (C_r) and additional higher symmetric and anti-symmetric modes appear.

Wave propagation characteristics are further complicated when a thin layer is attached to a thick medium. A RC beam with a CFRP layer is a good example of such a layered structure with two distinctively different thicknesses. Luangvilai et al. (2002) experimentally obtained the dispersion curve of a concrete beam with a CFRP layer and demonstrated the complexity of its wave propagation characteristics. Therefore, a conventional Lamb wave approach may not be applicable for the monitoring of CFRP-RC beam coupled structures, and a new approach, which can be used regardless of the complexity of waves, is necessary. To address this issue, the concept of TRA is proposed.

The origin of the proposed time reversal process traces back to TRA (Fink and Prada 2001). This time reversibility of acoustic (or body) waves has found applications in lithotripsy, ultrasonic brain surgery, nondestructive evaluation, and acoustic communications (Fink 1999). However, the time reversibility does not work well for guided waves due to their multimode and dispersion characteristics. A combination of a specific narrowband input waveform and multi-resolution signal processing is employed so that the time reversibility of guided waves is preserved within an acceptable tolerance for more complex configurations such as the layered structure presented in this study (Park et al. 2004). In the extended time reversal process, a narrowband input signal can be reconstructed at an excitation point (PZT A) if an output signal recorded at another point (PZT B) is reemitted to the original source point (PZT A) after being reversed and scaled in the time domain as shown in Figure 2. Interested readers are referred to Kim et al. (2006), where the extended time reversal process is described in detail.

Damage detection using the time reversal process is based on the premise that if there are certain types of defect along the wave propagation path, time reversibility breaks down. More precisely, the shape of the reconstructed signal's main wave packet will depart from that of the original input signal and the symmetry of the reconstructed signal is violated. By examining the deviation of the restored signal's main wave packet from the known input signal or the violation of the reconstructed signal's symmetry as shown in Figure 3, certain types of damage can be identified without requiring any previously obtained baseline signals. Based on this premise, two indices are proposed for damage identification: time reversibility (TR) and symmetry (SYM) indices. The TR index, defined below, compares the waveform of the original input with that of the reconstructed signal:

$$\mathrm{TR} = 1 - \sqrt{\left\{\int_{t_l}^{t_r} I(t)V(t)\,dt\right\}^2 \Bigg/ \left\{\int_{t_l}^{t_r} I(t)^2\,dt \int_{t_l}^{t_r} V(t)^2\,dt\right\}} \tag{1}$$

where *I(t)* and *V(t)* denote the known input signal and the main wave packet in the reconstructed signal, respectively. For the experimental study presented, a 7-peak toneburst signal is used for excitation; t_l and t_r represent the starting and ending time points of the toneburst signal as defined in Figure 3. The value of the TR index becomes zero when the shape of the main wave packet in the reconstructed signal is identical to that of the original input signal. Note that the amplitude scaling difference between *I(t)* and *V(t)* does not affect the TR value. If *V(t)* deviates from *I(t)*, the TR index value increases and approaches 1.0, indicating the existence of damage along the wave propagation path.

The SYM index measures the degree of symmetry of the reconstructed signal with respect to the main wave packet in the middle.

$$\mathrm{SYM} = 1 - \sqrt{\left\{\int_{t_o}^{t_r} L(-t)R(t)\,dt\right\}^2 \Bigg/ \left\{\int_{t_l}^{t_o} L(t)^2\,dt \int_{t_o}^{t_r} R(t)^2\,dt\right\}} \tag{2}$$

where *L(t)* and *R(t)* denote the left-hand and right-hand sides of the reconstructed signal with respect to the main wave packet, t_o is the center time point of the main wave packet and t_l and t_r represent the starting and ending time points as defined for the TR index. All terms are shown in Figure 3.

DESCRIPTIONS OF EXPERIMENTS

The overall configuration of the test specimens is shown in Figure 4. A total of five beams were tested for this study. Each RC beam was 254 mm deep, 152 mm wide and simply supported over 4750 mm. (The last three beams were supported over 3962 mm.) The beams were reinforced with 3 #4 (13 mm diameter) primary and 2 #3 (9 mm diameter) compression reinforcing bars. The soffit-applied preformed CFRP strip was 102 mm wide and 1.3 mm thick.

A total of 15 square PZT wafers (2 cm x 2 cm x 0.0508 cm) were attached on the free surface of the CFRP layer to form a distributed active sensing system (Figure 4(b)). For the time reversal process, the same data acquisition procedure was used as proposed by Kim et al. (2006). A chirp signal which has the frequency range from 1000 Hz to 50,000 Hz and one million sample rate were used for the impedance method. Each PZT wafer was actuated and sensed sequentially from PZTs #1 through #15 with the chirp signal. The infrared imaging system (IR in Figure 4(d)) is composed of the infrared camera (ThermaCAM S40), IR software (ThermaCAM Researcher Pro 2.7), 14 heat dishes and a protective device. The IR images were collected with 7 Hz sample rate and about 20 second time duration at each sensing zone from #1 to #14 up to 40.03 kN, which is the point where the loading condition is switched from the force-control to the displacement-control. After 40.03 kN, only sensing zones from #5 to #10 were scanned for reducing image collection time. Around from the loading step which initial debonding is suspected to start at, only the several suspicious sensing zones were inspected with the IR imaging technique.

The strain data acquisition system (DAQ2 in Figure 4(d)) includes four electrical resistance strain gauges on the internal reinforcing steel bars and four additional strain gauges mounted on the surface of the CFRP layer coincident with the previous strain gauges. These instruments were used to measure strains and to identify the presence of debonding at the discrete gauge locations. Details of the experimental setup and data analysis results based on strain measurements can be found in Reeve (2005) and Zorn (2006).

Four loading cases were investigated in this study (Cases IV-VII). Previous three cases (Case I-III) can be referred in Kim et al. (2006). In Case IV, The specimen was first subjected to fatigue loading in Case IV and subsequently to monotonic loading up to failure in Case V. In Case IV, a load range of 4.45 kN to 22.24 kN were applied. Different from the previous fatigue test, 2.0 Hz was chosen for the driving frequency of cyclic loads to reduce total experimental time. The specimen underwent a total of 2,000,000 fatigue load cycles over 14 days. Data from the active sensing system were gathered at several loading cycles: N = 0, 1, 100, 200, 500, 1000, 2000, 5000, 10000, 300000, 450000, 600000, 707000, 900000, 1040000, 1210000, 1392000, 1540000, 1700000, 1840000, 2000000 cycles. During the data collection from the active sensing system: time reversal data and Impedance data, the cyclic load was paused at the minimum load of 4.45 kN. The IR imaging technique was not used in the Case IV.

A monotonic load test similar to Cases I, III, VI and VII was performed on the first specimen following the fatigue-conditioning described above. This was referred to as Case V. the specimen was subjected to incremental monotonic loading, and the data from the active sensing system were collected at each loading step. The monotonic load was gradually increased until the specimen failed. The loading was initially force-controlled up to loading step 4 (36.94 kN) and then switched to a displacement control from loading step 5 (42.05 KN) to loading step 12 (64.53 kN). Time reversal signals, impedance data and thermal images were collected at each 12 loading step.

As conducted in Case V, two specimens were also subjected to incremental monotonic loadings in Case VI and VII. The force-controlled was used up to loading step 5 (40.05kN) and then switched to a displacement control from loading step 6 (44.14 KN) to loading step 10 (58.47 kN) and 16 (46.28 kN), respectively. Time reversal signals, impedance data and thermal images were collected at each 10 loading step in the Case VI. However, because of the safety of the thermal camera, the IR images were captured only after the completion of the test in the Case VII.

The prior two cases (Case IV and V) and the latter two cases (Case VI and VII) underwent the similar procedures to previous Case II-III and Case I in Kim et al. (2006), respectively. For all cases, the loading was applied at the mid-point of the simply supported beam, and during the data collection in the force-control and the fatigue loading conditions, data from the active sensing devices were collected while the load was held constant. In the displacement control, data were collected continuously without a pause.

EXPERIMENTAL RESULTS

Additional one fatigue and three monotonic load tests (Cases IV-VII) were conducted on three CFRP strengthened RC beams to verify the time reversal method which could have been successfully applied to the same type of specimens in the previous tests (Case I-III). Experimental results based on the measured data are presented in this section for all cases (Cases I-VII).

Case I-III: Monotonic, Fatigue, Monotonic after fatigue loading in the previous tests

The damage diagnosis obtained in the previous loading tests of the first and second CFRP-RC beam specimens is presented in Figure 5, Figure 6, Figure 7 and Figure 8. In Figure 5, the TR and SYM indices are shown along the length of the beam and computed at selective loading steps (loading steps 1, 2, 6, 7, 15 and 24). As previously mentioned in Kim et al. (2006), the initial increases of the TR and SYM indices at the mid-span did not result from debonding but rather from initial cracking of the concrete beam by a 4.8 mm diameter steel rod. This initial increase of indices could be removed by getting rid of the rod in the Case IV-VII. Different results could be seen in the next section. The TR and SYM indices values at sensing zones 10 and 14 are plotted as a function of the 24 loading steps in Figure 6. Figure 6 shows that the TR and SYM indices significantly increased at loading step 5 near sensing zone 10. Overall, the findings in the Case I agreed well with visual inspection or a coin-tapping test performed after the completion of the monotonic load test and the data obtained from the strain gauge system (Reeve 2005). The second specimen was subjected to the fatigue loading of the Case II. Different from the Case I, Case II showed no sign of CFRP strip debonding from the substrate concrete beam during the test nor any evidence of debonding found from visual inspection or a coin tapping test performed following the fatigue loading test. In Case III, it was also successfully found that the debonding was initiated after the loading step 11 near sensing zone 10 based on the TR and SYM indices shown in Figure 7 and Figure 8. Furthermore, Case III showed the possibility that proposed method could provide an earlier warning of debonding than detailed visual inspection by generating increased index values at the invisible debonding stages.

Case IV-VII: Fatigue, Monotonic after fatigue, two Monotonic loadings in the present tests

Firstly, the specimen of Case IV was subjected to the fatigue loading of the Case IV. As the result from the previous fatigue loading test of Case II, no sign or evidence of CFRP debonding from the concrete beam could be found during the test in the Case IV.

For all three monotonic loading cases (Cases V, VI and VII), the approximate debonding locations that were found from visual inspection and a coin tapping test performed after the test are shown in Figure 9. As Cases V-VII are basically the same type of monotonic loading tests as Case I and III, they showed qualitatively similar tendency of results as in Case I and III. In all Cases V, VI and VIII, debondings started from around sensing zone 9 and propagated to the end of the beam (sensing zone 14), and they initiated from loading steps 10, 10 and 13, respectively. Therefore, the damage diagnosis based on the results from the Case VII is only presented as the representative of all monotonic loading cases.

Time Reversal Method

Figure 10 shows changes of the TR and SYM indices measured at 6 loading steps (1, 7, 13, 14, 15 and 16) during the Case VII monotonic loading test. Different from the Figure 5 and Figure 7, the initial increases of the TR and SYM indices at the mid-span could not be seen in Figure 10. From this result, it is verified that the initial cracking of the concrete beam by the steel rod caused the abnormal index values in the middle of the beam. Also, huge TR and SYM indices could been expected at the sensing zones from 9 through 13 in Figure 10 based on the actual debonding locations in Figure 9(c). However, only a few parts of debonding zones show increased index values, and the TR and SYM indices of the same loading step are not consistent even at the same sensing zone. For example, the TR index value of Step 16 is over 0.4 at the sensing zone 11 but the SYM index is almost zero at the same loading step and sensing zone.

This kind of tendency of index values can be also seen in the Figure 11, which plotted the TR and SYM indices values at sensing zones 9 and 1 as a function of the 16 loading steps. Debonding initiated from sensing zone 9, and sensing zone 1 is located at the end of the beam where no debonding is expected. Figure 11 shows that: (1) the TR and SYM indices significantly increased at loading step 12 and 11 near sensing zone 9, but after that, they decreased and came back to the original values finally; and (2) they did not vary much near sensing zone 14 throughout the entire loading steps as also reported in the previous Cases I and III. The sudden increase of the TR and SYM indices right before the initiation of the debonding is in good agreement with the previous test results from the Case III (monotonic loading test after the fatigue test). However, decreased TR and SYM indices could not be seen in the previous test Cases.

This kind of different behavior might have been resulted from the initial bonding condition between CFRP strips and substrate concrete beams. In the previous test Case I-III, relatively more sufficient portion of the epoxy adhesive was used for the bonding layer and the surface of the concrete specimens was better grinded by a skilled technician before attaching the CFRP strips on the concrete beams than in the test Cases IV-VII. Therefore, in these cases (Case IV-VII), it is suspected that the bonding condition has not been good enough that debonding (breaking the bonding condition) could generate the nonlinear behavior between two layers and this resulted in small index values in debonding zones.

Impedance Method

Figure 12 shows changes of the impedance values measured at two loading steps (1 and 15) during the Case VII monotonic loading test and after the test at the location of PZTs #9 and #12. Partial debonding could not generate impedance peaks in Figure 12(a). Note that the sensing zones 9 and 13 are partially debonded zones and 10 to 12 are fully debonded zones identified by the visual inspection and a coin tapping test in Figure 9(c). However, impedance peaks can be seen on a completely detached zone (sensing zone 12) as shown in Figure 12(b). Different from the TR and SYM indices which depend on whether the generation of the material nonlinearity resulted from the debonding or not, impedance method can detect fully debonded zones with the impedance peaks generated by the resonance frequencies regardless of the nonlinearity of the material. In spite of this kind of advantage, impedance method could not detect partial or slightly touched debonding during the test even though the debonding already had occurred. As shown in Figure 12(b), debonding could be found only after the completion of the test, not even at the loading step 16 which is definitely a debonded stage. Note that the beam was taken down from the frame and flipped over on the floor after the test. “After test” data were collected in this condition. Thus, impedance method might not be able to provide a good indication about the initiation of debonding.

Infrared Imaging Technique

Results from the infrared thermal images are shown in Figure 13 and Figure 14. IR images present a good indication of debonding areas as shown in Figure 13 and Figure 14(b) after the completion of the test. However, like the impedance method, the IR imaging technique could not show good images for the debonding zones while the test specimens were being loaded. As shown in Figure 14(a), it is not easy to identify the debonding area during the test, compared with the IR image in Figure 14(b).

CONCLUSION

In this study, previous experimental results are verified by new data which were obtained by the same continuous monitoring system for detecting CFRP debonding. Also, results from another NDT techniques are compared for validate the proposed monitoring system. This *baseline-free* nondestructive testing (NDT) technique was demonstrated by the seven loading cases of five CFRP strengthened RC beams tests: three monotonic load tests (Cases I, VI and VII), two fatigue load tests (Case II and IV), and two monotonic tests following the fatigue load tests (Cases III and V). This approach successfully estimated the initiation and region of debonding in Cases I-III. However, in Cases IV-VII, only the initiation of debonding could be detected. This kind of different results between two test groups might have been resulted from the initial bonding condition between CFRP strips and substrate concrete beams. In the Cases IV-VII, it is suspected that the poor bonding condition could not generate the nonlinear behavior between the two layers. Even though a specimen has a remarkable portion of the fully debonded zones as shown in Figure 15, the proposed method cannot detect the debonding as long as damages do not make nonlinearity between the CFRP and the concrete layers.

It is considered that the impedance method and the IR imaging technique could only detect fully untouched debonding areas which have sufficient gap between the layers. Also, these methods could not identify the initiation of debonding and detect debonding zones during the test even when huge debonding zones were visible. From the all results, it is expected that the proposed reference-free NDT technique could be successfully used for detecting the initiation of debonding.

ACKNOWLEDGEMENTS

This research was partially supported by an NSF Grant No. CMS-0529208 and Pennsylvania Infrastructure Technology Alliance (PITA) program. The authors would like to thank the CMS Program Manager, Dr. Shi Lui and the PITA co-director, Prof. Cristina Amon for their supports. The authors also like to thank Seung Bum Kim and Dena E. De Iuliis for assisting our experiments. The first author would like to acknowledge the Electric Power National Scholarship Program at the Ministry of Commerce, Industry and Energy (MOCIE) in Gwachon, South Korea. The beam testing was conducted by Andrew Zorn and Benjamin Reeve in the Watkins-Haggart Structural Engineering Laboratory at the University of Pittsburgh.

REFERENCES

Akuthota, B., Hughes, D., Zoughi, R., Myers, J., and Nanni, A. (2004). “Near-Field Microwave Detection of Disbond in Carbon Fiber Reinforced Polymer Composites Used for Strengthening Cement-Based Structures and Disbond Repair Verification.” *J. of Mater. in Civil Eng.*, 16(6), 540-546.

Ansari, F. (2005). “Fiber optic health monitoring of civil structures using long gage and acoustic sensors.” *Smart Mater. and Struct.*, 14(3), S1-S7.

Ekenel, M., Stephen, V., Myers, J. J., and Zoughi, R. (2004). “Microwave NDE of RC Beams Strengthened with CFRP Laminates Containing Surface Defects and Tested Under Cyclic Loading.” *Proc., 16th World Conference on Nondestructive Testing*, Montreal, Canada. August 30- September 3.

Feng, M. Q., Flaviis, F., and Kim, Y. J. (2000a). ‘‘Use of Microwaves for Damage Detection of Fiber Reinforced Polymer-Wrapped Concrete Structure.’’ *J. Eng. Mech.*, 128(2), 172–183.

Fink, M. (1999). “Time-Reversed Acoustics.” *Scientific American*, 281(5), 91-97.

Fink, M., and Prada, C. (2001). “Acoustic Time-Reversal Mirrors.” *Inverse Problems*, 17, R1-R38.

Giurgiutiu, V., Harries, K.A., Petrou, M.F., Bost, J., and Quattlebaum, J. (2003). “Disbond Detection with Piezoelectric Wafer Active Sensors in RC Structures Strengthened with FRP Composite Overlays.” *Earthquake Eng. and Eng. Vibration*, 2(2), 213-224.

Giurgiutiu, V., and Lyshevski, S.E. (2004). *Micromechatronics: Modeling, analysis, and design with MATLAB*, CRC Press Inc, Boca Raton, FL.

Hong, S., and Harichandran, R. (2005). “Sensors to Monitor CFRP/Concrete Bond in Beams Using Electrochemical Impedance Spectroscopy.” *J. of Composite for Construction*, 9(6), 515-523.

Ing, R.K., and Fink, M. (1996). “Time Recompression of Dispersive Lamb Waves using a Time Reversal Mirror – Application to Flaw Detection in Thin Plates.” *Proc., 1996 IEEE Ultrasonics Symposium*, 1, 659-663.

Karbhari, V.M., Chin, J.W., and Reynaud, D. (2000). “Critical Gaps in Durability Data for FRP Composites in Civil Infrastructure.” *Proc., 45^{th} International Society for the Advancement of Materials and Process Engineering (SAMPE) Symposium and Exhibition*, Vol. 45, 549-563, Long Beach, CA, May 21-25.

Kessler, S. S., Johnson, C. E., and Dunn, C. T. (2003). “Experimental application of optimized Lamb wave actuating/sensing patches for health monitoring of composite structures.” *Proc., of the 4th International Workshop on Structural Health Monitoring*, Stanford University, 429-436.

Kim, S., Sohn, H., Greve, D., and Oppenheim, I. (2005). “Application of a Time Reversal Process for Baseline-Free Monitoring of a Bridge Steel Girder.” *Proc., International Workshop on Structural health monitoring*, Stanford, CA, September 15-17.

Kim, S., In, C., Cronin, K., Sohn, H. and Harries K. (2006). “A Reference-Free NDT Technique for Debonding Detection in CFRP Strengthened RC Structures.” *ASCE J. of Structural Engineering*, in press.

Levar, J. and Hamilton, H. (2003). “Nondestructive Evaluation of Carbon Fiber-Reinforced Polymer-Concrete Bond Using Infrared Thermography.” *ACI Mater. J.*, 100(1), 63-72.

Luangvilai, K., Punurai, W., and Jacobs, L. (2002). “Guided Lamb Wave Propagation in Composite Plate/Concrete Component.” *J. of Eng Mech.*, 128(12), 1337-1341.

Mal, A. K., Shih, F. J., Ricci, F., and Sauvik, B. (2005). “Impact damage detection in composite structures using Lamb waves.” *Proc., of the SPIE*, 5768, 295-303.

Mirmiran, A., Shahawy, M., and Echary, H. (1999). “Acoustic Emission Monitoring of Hybrid FRP-Concrete Columns.” *J. of Eng. Mech.*, 125(8), 899-905.

Mirmiran, A., and Wei, Y. (2001). “Damage Assessment of FRP-Encased Concrete Using Ultrasonic Pulse Velocity.” *J. of Eng. Mech.*, 127(2), 126-135.

Park, H.W., Sohn, H., Law, K.H., Farrar, C.R. (2004). “Time Reversal Active Sensing for Health Monitoring of a Composite Plate.” *J. of Sound and Vibration*, in press.

Reeve, B. (2005). “Effect of Adhesive Stiffness and CFRP Geometry on the Behavior of Externally Bonded CFRP Retrofit Measures Subject to Monotonic Loads.” MS Thesis, University of Pittsburgh Department of Civil and Environmental Engineering.

Rose, L. J. (1999). *Ultrasonic Waves in Solid Media*, Cambridge University Press, New York.

Sohn, H., (2006). “Effects of Environmental and Operational Variability on Structural Health Monitoring,” *a Special Issue of Philosophical Transactions of the Royal Society on Structural Health Monitoring*, in press.

Sohn, H., Park, H., Law, K., and Farrar, C. (2006). “Combination of a Time Reversal Process and a Consecutive Outlier Analysis for Baseline-free Damage Diagnosis,” *J. of Intelligent Mater. Systems and Structures*, in press.

Viktorov, I.A. (1967). *Rayleigh and Lamb Waves*, Plenum Press, New York.

Zorn, A. (2006). “Effect of Adhesive Stiffness and CFRP Geometry on the Behavior of Externally Bonded CFRP Retrofit Measures Subject to Fatigue Loads.” MS Thesis, University of Pittsburgh Department of Civil and Environmental Engineering.

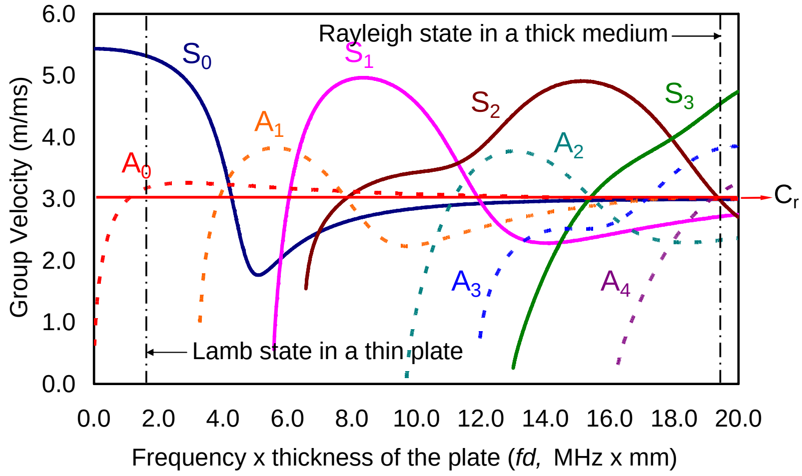

Figure 1: A typical dispersion curve of Lamb wave in a thin plate

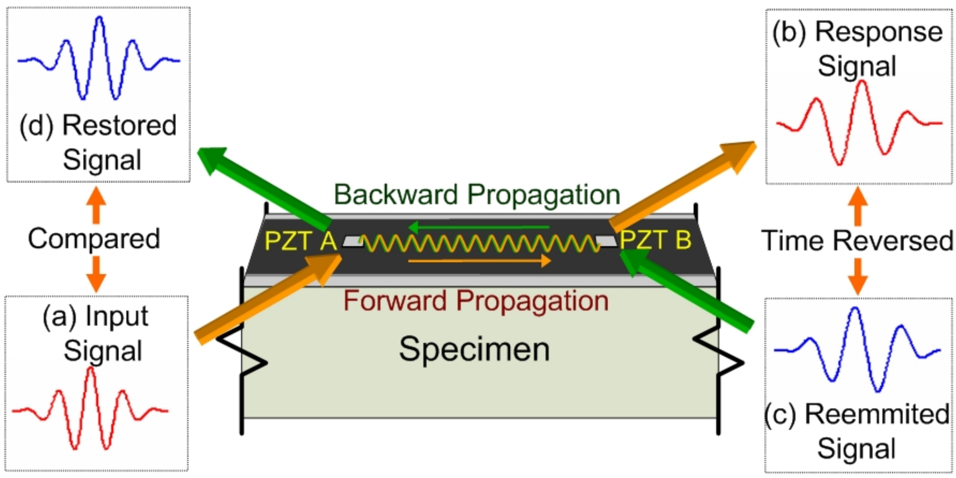

Figure 2: Schematic concept of TRA-based damage identification that does not require any pas baseline signals: (a) a known input signal is applied to PZT A, (b) the corresponding response is measured at PZT B, (c) the response at PZT B is reversed in the time domain and applied back to PZT B, and (d) the final response is measured at PZT A. The shape of this reconstructed signal should be identical to the original input signal without defect along the wave propagation path.

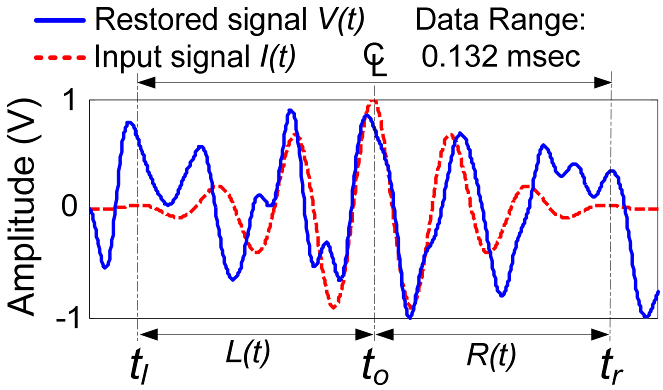

Figure 3: Definition of t_l, t_o, and t_r used in Equation (1) & (2)

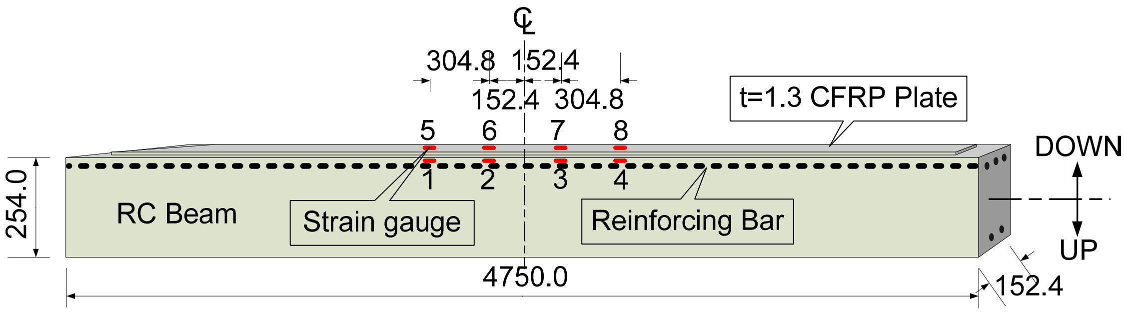

(a) Elevation of a CFRP strengthened RC beam with strain gauge locations (shown upside down)

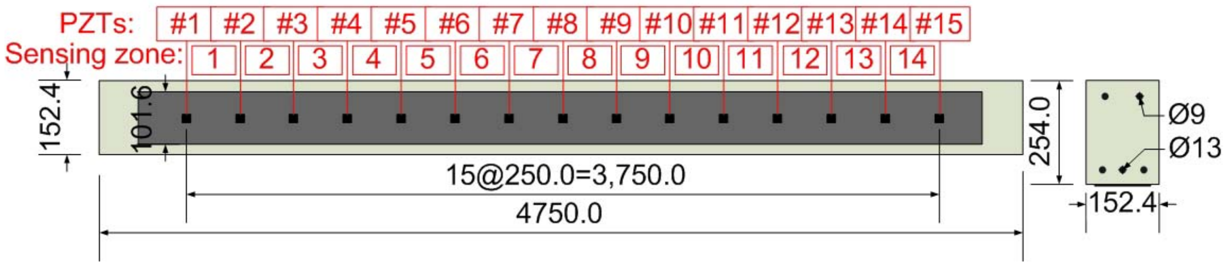

(b) An inverted plan view of the CFRP strengthened RC beam showing the PZT sensors and the sensing zones

(c) Testing configuration

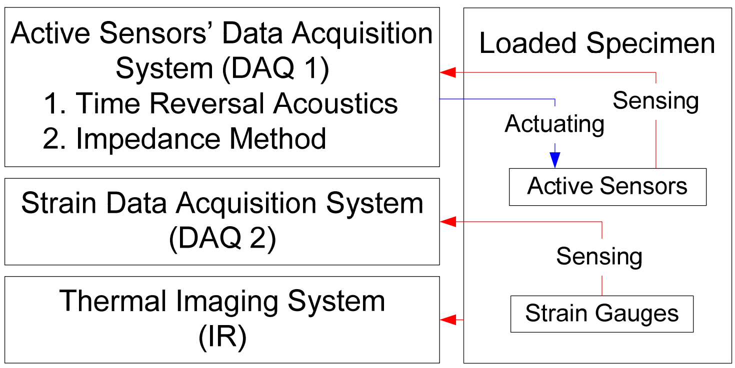

(d) A layout of the active sensing data acquisition

Figure 4: Test setup and configuration of strain gauge and active sensing devices embedded/attached to the CFRP strengthened RC beam (all units are in mm)

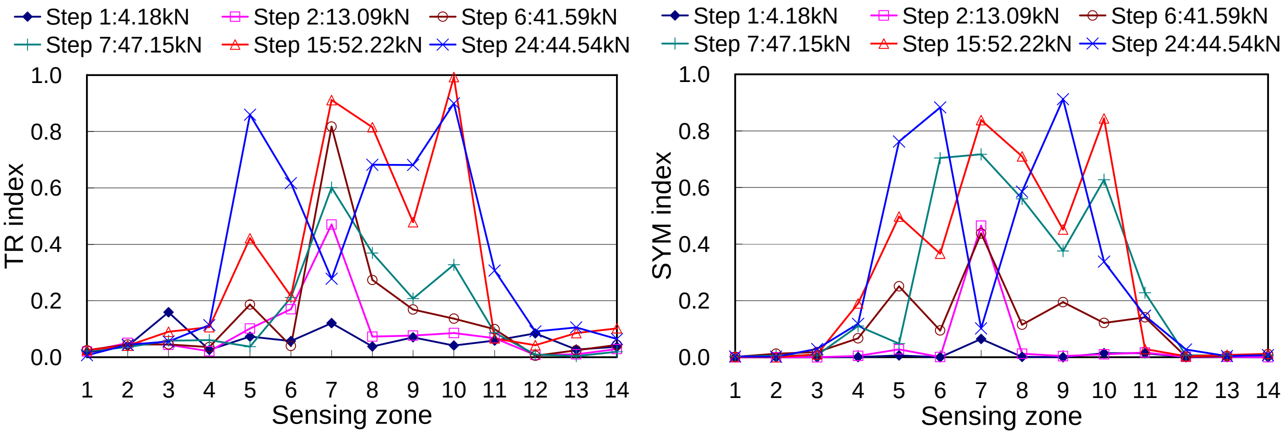

(a) TR indices at 6 selective loading steps

(b) SYM indices at 6 selective loading steps

Figure 5: Changes of the TR and SYM indices measured at selective loading steps during the Case I monotonic loading test

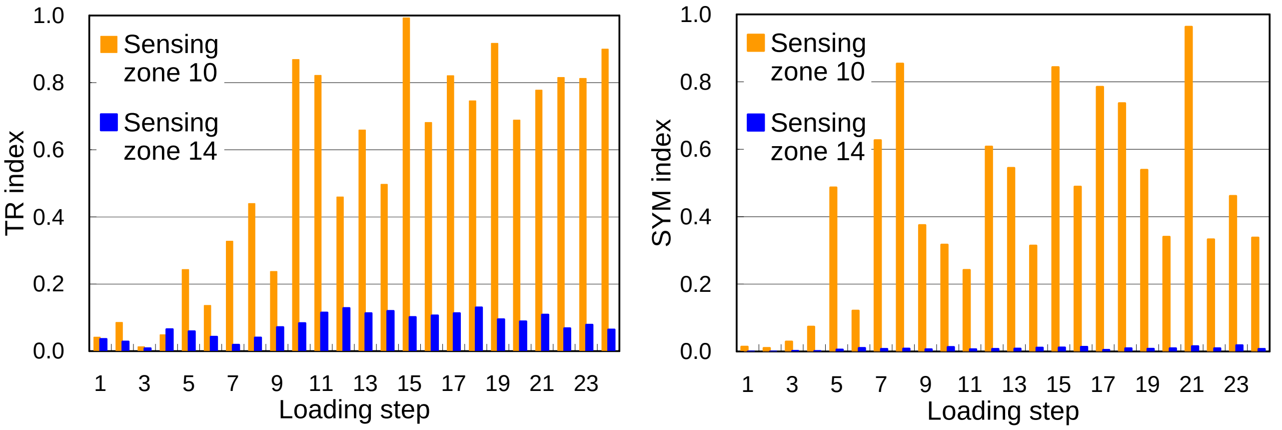

(a) TR indices at sensing zones 10 and 14

(b) SYM indices at sensing zones 10 and 14

Figure 6: Changes of TR and SYM indices as a function of incremental monotonic loading measured at sensing zones 10 and 14 for Case I

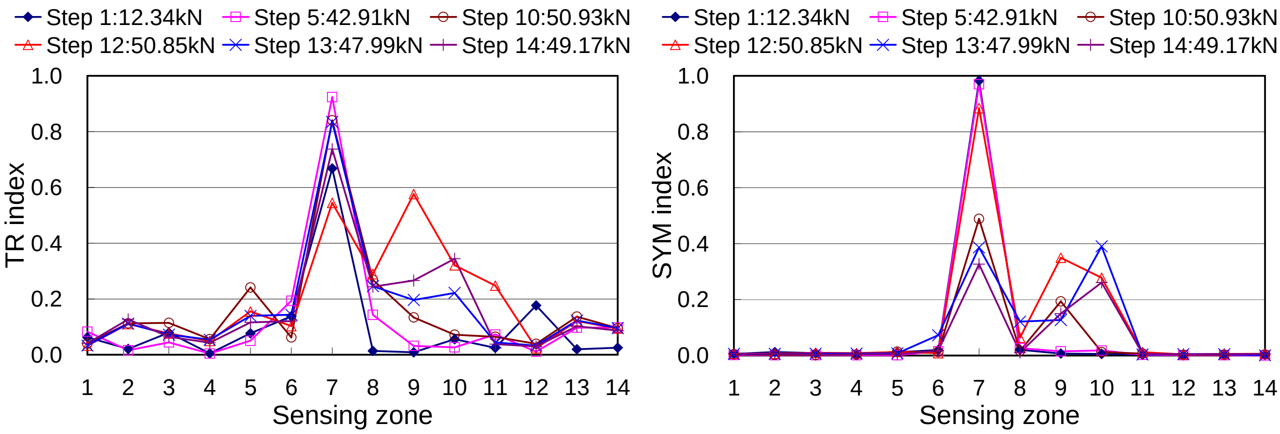

(a) TR indices at 6 loading steps

(b) SYM indices at 6 loading steps

Figure 7: Changes of the TR and SYM indices measured at selective loading steps during the Case III monotonic loading test

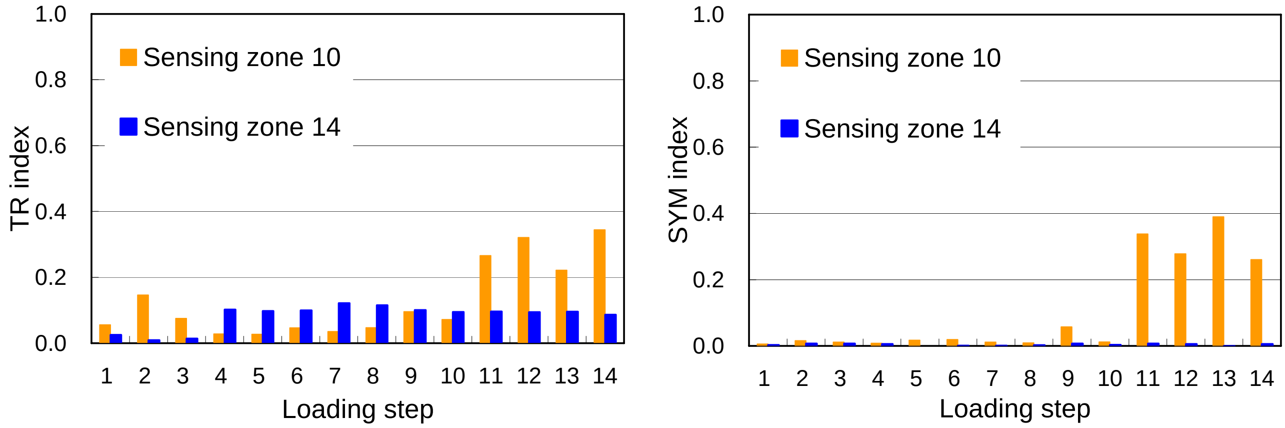

(a) TR indices at PZTs #10-#11 and #14-#15

(b) SYM indices at PZTs #10-#11 and #14-#15

Figure 8: Change of the TR and SYM indices as a function of increasing monotonic loading measured at sensing zone 10 and 14 for Case III

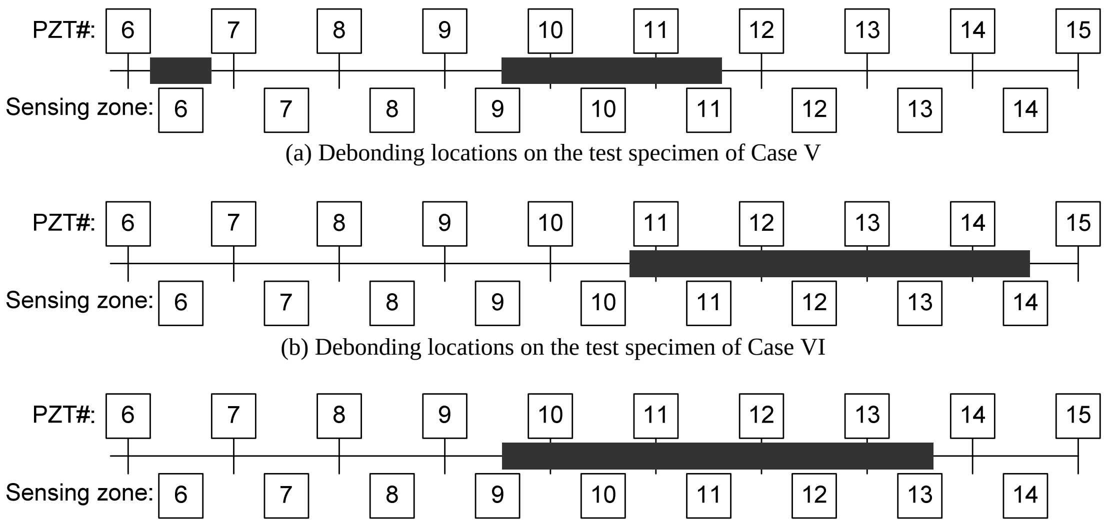

(a) Debonding locations on the test specimen of Case V

(b) Debonding locations on the test specimen of Case VI

(c) Debonding locations on the test specimen of Case VII

Figure 9: Approximately identified debonding locations from visual inspection and a coin tapping test performed after the test Cases V-VII

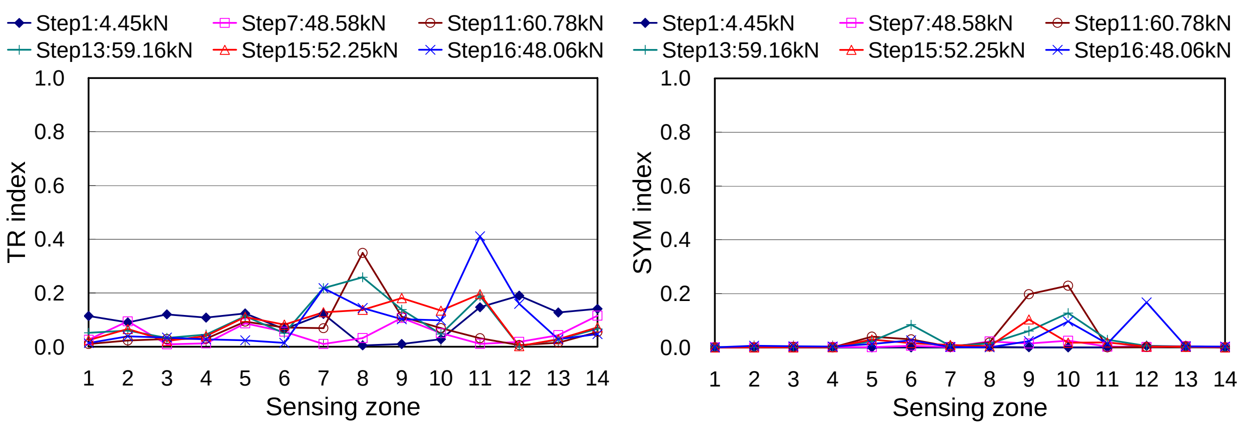

(a) TR indices at 6 loading steps

(b) SYM indices at 6 loading steps

Figure 10: Changes of the TR and SYM indices measured at selective loading steps during the Case VII monotonic loading test

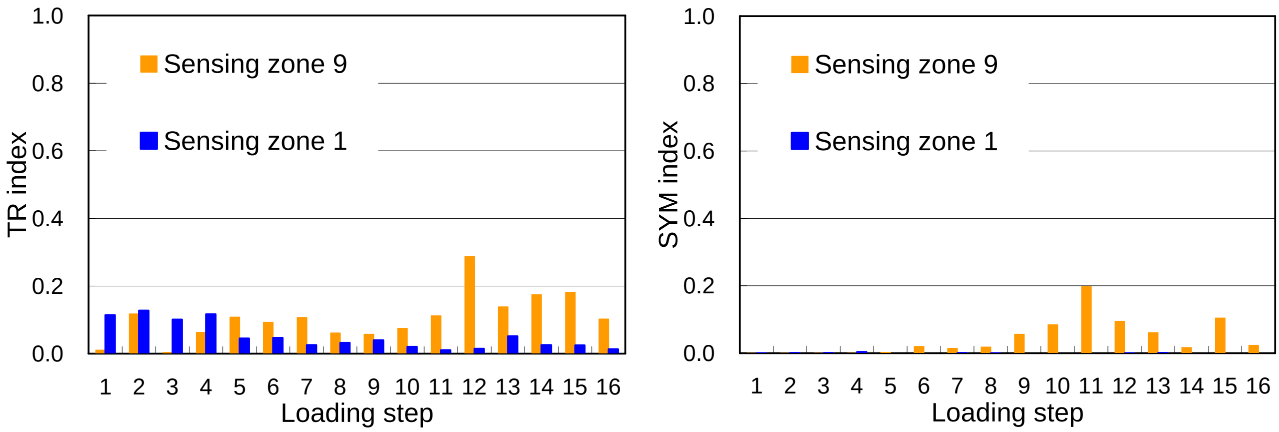

(a) TR indices at PZTs #9-#10 and #1-#2 (b) SYM indices at PZTs #9-#10 and #1-#2

Figure 11: Change of the TR and SYM indices as a function of increasing monotonic loading measured at sensing zone 9 and 1 for Case VII

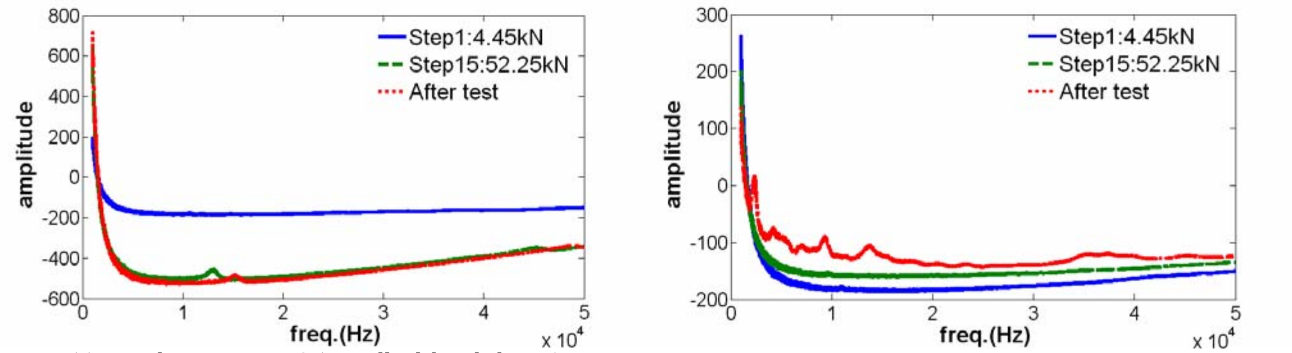

(a) Impedance at PZT #9 (partially debonded zone) (b) Impedance at PZT #12 (fully debonded zone)

Figure 12: Changes of the impedances measured at loading steps 1 and 15 and after the Case VII monotonic loading test

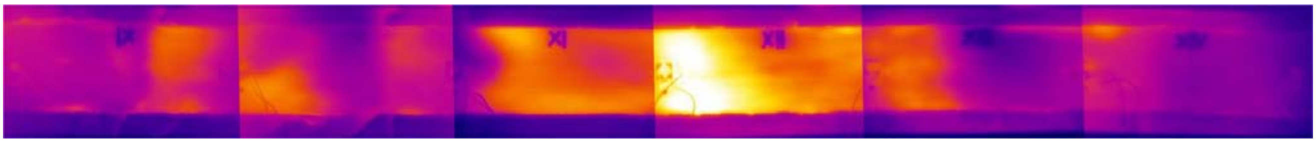

Figure 13: Identified debonding zones by the infrared (IR) camera after the Case VII monotonic loading test

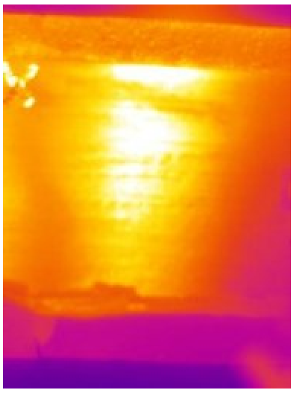

(a) IR image at loading step 10 right after the debonding occurred

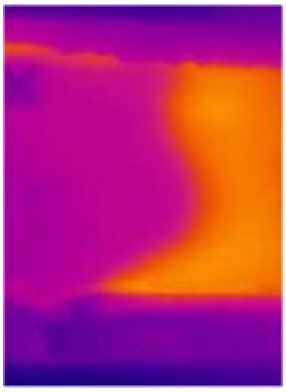

(b) IR image after the test (the beam was flipped over)

Figure 14: Comparison of IR images at sensing zone 10 right after the debonding occurred with after the test in Case VI

Figure 15: Fully and cleanly debonded zones underneath the specimen of the Case VI monotonic test